

In-flight RCS measurements of drones and birds at K-band and W-band

Samiur Rahman^{1*}, Duncan A. Robertson¹

¹ SUPA School of Physics and Astronomy, University of St Andrews, St Andrews, Fife KY16 9SS, Scotland

*sr206@st-andrews.ac.uk

Abstract: This paper presents in-flight Radar Cross Section (RCS) data of drones and birds at K-band and W-band obtained from extensive experimental trials. The focus of the paper is to demonstrate the RCS characteristics of these targets in practical scenarios, hence experimental results are used exclusively. Due to variations in orientation, aspect angle and target motion, the measured RCS values of these targets fluctuate significantly during their flight. Three very well calibrated Frequency Modulated Continuous Wave (FMCW) radar systems, one operating at K-band (24 GHz) and two at W-band (94 GHz), have been used to collect data for RCS analysis. Three drones of different sizes (DJI Phantom 3 Standard, DJI Inspire 1 and DJI S900 Hexacopter) and four birds of prey of different sizes (Northern Hawk Owl, Harris Hawk, Indian Eagle Owl and Tawny Eagle) have been used for data collection. The results demonstrate that the RCS scales broadly with the size of the target, consistent with the optical scattering regime, and that the RCS values for each target are comparable at K-band and W-band. The statistical distribution of RCS for each target falls within a certain range which is useful for predicting the performance of a drone detection radar.

1. Introduction

Commercial drones have recently become very easily obtainable by the public. It has been estimated that the use of drones will triple by the year 2020 [1]. Drones offer numerous advantages in the modern society in terms of transportation, high quality video and imagery, assistance with rescue operations etc. On the other hand, as drones are not well regulated yet, they can easily be used with malicious intent. Examples of nefarious use include contraband or explosive transport, illegal video streaming, flying in restricted airspace and taking photographs of critical national structures. Hence, the requirement for drone detection sensors has become a necessity in the current context and radar offers a powerful solution.

A practical problem which a drone detection radar would face is that birds could be the cause of false alarms. Hence, the radar system should be able to discriminate between drones and birds. A millimetre wave radar can be very suitable as a drone detection system due to the high Doppler sensitivity in this frequency band, which consequently produces high fidelity micro-Doppler signatures [2]. Hence, it is of practical importance from a system design point of view to study the RCS of drones and birds (the main confusers) at millimetre wave frequencies. There have been very few reports on drone and bird RCS so far in the microwave frequencies and almost none in the millimetre wave. Most of the reports in terms of drone detection radar systems have mainly focused on the micro-Doppler properties [3]–[5]. In [6], [7], numerical and experimental results of a commercial drone RCS were reported for the first time. In [6], the RCS analysis was performed for a DJI Phantom 2 at X-band (10 GHz). Numerical modelling of the drone was done using the finite element method [8] and method of moments [9]. The modelling results were verified by experimental results obtained from anechoic chamber data. The drone RCS was found to be on average -20 dBsm, after accounting for the fluctuations at different aspect angles. In [7], the RCS analysis was performed only for the rotor blade of a DJI

Phantom Vision 2 Plus at S-band (2.4 GHz). For RCS prediction, the Finite-Difference Time-Domain (FDTD) method [10] was used. Experimental results were also obtained from anechoic chamber data. The modelling was done by assuming an aluminium rotor blade and the anechoic chamber experiments were performed with carbon fibre, plastic and metallic blades.

In terms of bird RCS, the amount of literature available is again quite small and we are unaware of any reports at millimetre wave frequencies. In [11], bird RCS is mentioned to be around -20 dBsm but it should be noted that this value does not consider the variations due to frequency or aspect angle. In [12], very crude RCS measurements of ducks and chickens were performed in a lab environment, using polyfoam supports to position the live birds. In [13], numerical modelling of a bat was performed at X-band and experimental measurements were made on a suspended dead Brazilian free-tailed bat specimen. The measured RCS values varied from -45 to -35 dBsm. In-flight measurements of birds at X-band were reported in [14] and relative RCS values were calculated. The relative RCS values of the body and wings of a flying mallard duck have been extracted from K-band micro-Doppler signatures in [15] using a similar method to [14].

In this paper, the aim is to generate a catalogue of measured in-flight RCS values of drones and birds of varying sizes at K-band and W-band. As discussed so far, the academic resource is very limited in terms of RCS values of these targets at frequencies above X-band. Numerical modelling of electromagnetic scattering from complex structures at both these high frequencies is computationally expensive and time consuming. Comparisons between simulated and measured RCS values at lower frequencies have shown only general agreement [6]. Our approach has therefore been to collect measured data from in-flight targets using well calibrated radars. A range of target types and sizes has been used to provide a robust data set. The resulting data set is considered to be more realistic of an operational

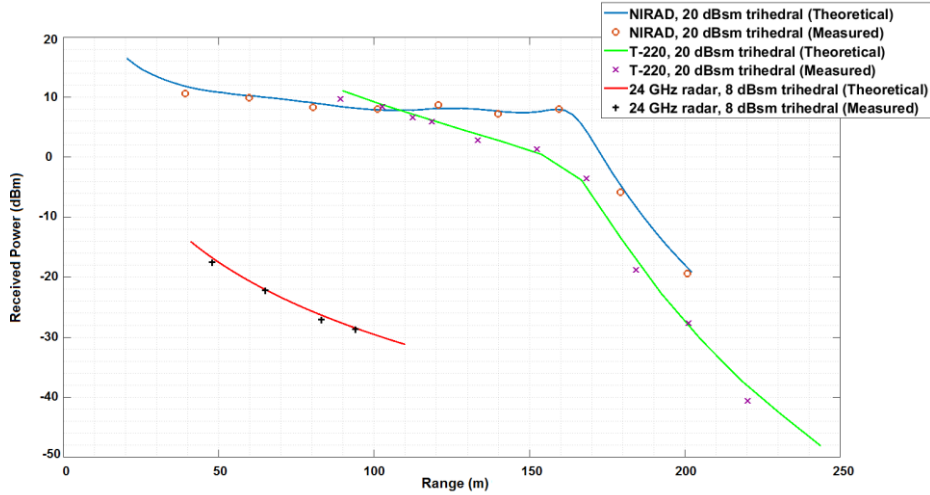


Figure 1: Calibration curves of the three radars (NIRAD, T-220 and 24 GHz radar) obtained by measuring the signal return from a known precision trihedral (19.7 dBsm at 94 GHz and 7.9 dBsm at 24 GHz)

scenario for a drone detection radar than might be obtained from either anechoic chamber measurements or numerical simulations.

Section 2 of this paper discusses the RCS measurement methodology, describing the experimental scenario and technical details of the radar systems used. Section 3 shows RCS results of the three drones in both hovering and flying scenarios, obtained from radars operating at 24 GHz and 94 GHz. Section 4 then presents in-flight RCS values of the four birds at the two radar frequencies. We do not present any measurements for stationary birds as it would not be possible to decouple the scattering contribution of the perch from that of the bird. Section 5 provides a concise summary and analysis of the overall data. Finally, concluding remarks in light of the processed results are given in Section 6.

2. RCS measurement and experimental method

The first step during the experimental trial has been to ensure that all the radars are well calibrated. These calibration curves are then used to calculate the target RCS from the received power. For W-band measurements, two 94 GHz radars have been used during the experimental trials. One is a low phase noise, heterodyne architecture based 94 GHz FMCW radar, called NIRAD [16]. The radar transmit power is +20 dBm. It has a circular polarized (CP), 42.5 dBi gain single pencil beam antenna (0.74° azimuth and 0.8° elevation beamwidths). Due to very narrow beamwidth in both azimuth and elevation, NIRAD has only been used for hovering target measurement. The second one is a very low phase noise, homodyne architecture based, 94 GHz FMCW radar, called T-220 [17]. This radar has a dual fan beam antenna (0.9° azimuth and 3° elevation beamwidths) with 40.5 dBi gain and is circular polarized. The radar transmit power is +18 dBm. Both the radars use an upconverted and multiplied Direct Digital Synthesizer (DDS) frequency modulation source and are phase coherent. For K-band measurements, a Phase Locked Loop (PLL) based 24 GHz phase coherent FMCW radar has been built based around an Analog Devices 24 GHz radar transceiver evaluation board [18]. Three 24.5 dBi gain horn antennas (11.2° azimuth and 11.2° elevation beamwidths)

have also been designed and built in house. As the maximum transmit power available from the evaluation board is only +8 dBm, a power amplifier with an output power of +24 dBm has been added to achieve better range coverage. The 24 GHz radar can be configured for different linear polarisations but we had preselected to use horizontal polarisation (HH) as this is known to maximise the return from horizontally aligned propeller blades [7]. All three radars are operated with a Graphical User Interface (GUI) written in National Instruments LabWindows/CVI which provides a live update of the range profile and range-Doppler image during data collection. All three radars were configured to use a 150 MHz chirp bandwidth yielding a range resolution of 1 m.

The radars were calibrated as a function of range using a precision trihedral with an edge length of 123 mm which provides an RCS of 19.7 dBsm at 94 GHz and 7.9 dBsm at 24 GHz. The trihedral was mounted on a tripod-supported 3 m long plastic pole to minimise ground clutter and the trihedral was aligned carefully to maximise the reflected power. The received power was measured at various ranges between 40 and 220 m. The data were then fitted with curves derived from the radar range equation [19] which had been modified to account for the frequency dependent gains of each system. For amplitude accuracy a Flattop window was used in the FMCW Fast Fourier Transform (FFT) and the relevant window gain correction applied.

The results in Fig. 1 show all three radars are well calibrated: all the radars show agreement between the measured points and the model within ± 1 dB, apart from the farthest range measurement with T-220 (possibly due to a slight measurement error at long range). The response of the 24 GHz radar follows the classical $1/R^4$ curve as it has no additional frequency dependent filter. The curve for NIRAD is flattened over much of the range due to an R^3 filter in the receiver chain. Both NIRAD and T-220 have baseband anti-alias low-pass filters which are responsible for the rapid fall off in received power at longer ranges. To get the best fit, 1 dB is added to the NIRAD measured values, whereas 1.5 dB is added to the T-220 and 24 GHz radar values. This small offset mainly accounts for cable/insertion loss and slight difference between the datasheet and measured values. With this offset compensation, all the calibration curves fit the

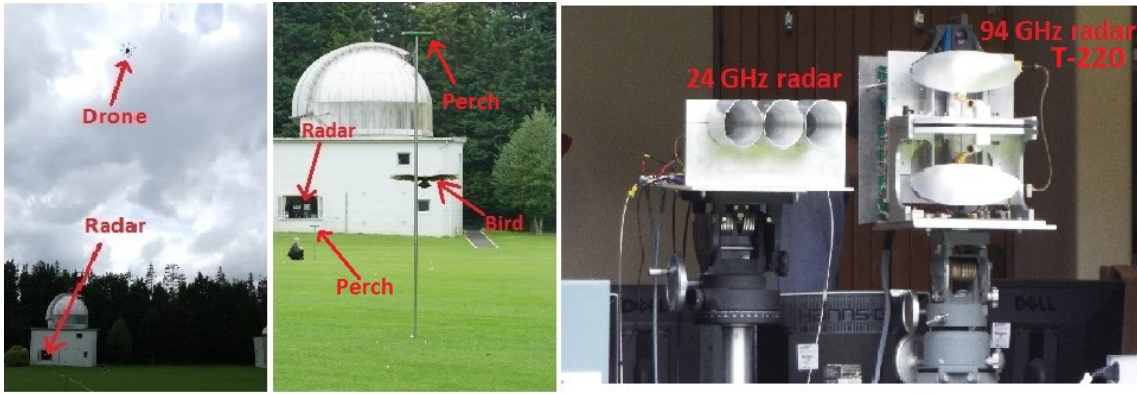


Figure 2: Experimental scenario for the RCS measurements of the drones and birds along with two of the radars used during data collection. Drone measurement (left), bird measurement (middle) and the 24 GHz and 94 GHz radars used during data collection)

measured values very well and can be used to predict the expected received power as a function range and from that derive the RCS. During calibration of all the radars, the antenna pointing was adjusted to maximise the return signal from the trihedral. As the elevation beamwidth of the 24 GHz antennas is larger than that of the W-band antennas, the K-band radar was receiving ground clutter reflections beyond 94 m despite being tilted up in elevation (approximately 3°). Hence, the 24 GHz radar does not have measured values after this range. This issue of ground clutter return must also be considered during RCS measurements of the flying targets, especially the birds (discussed later in this section).

The experimental data collection was performed separately for drones and birds. On every data collection day, the absolute power level of the radar noise floor and the power received from a trihedral at a known range was cross-

checked against the calibration curve to verify correct operation. Fig. 2 shows the experimental setup at the University of St Andrews Observatory. The radars point out of the lab window over an open grass covered area above which the targets flew/hovered.

For drones, data was first collected with the target hovering at various elevations. In this case the antennas were boresighted on the target to ensure well calibrated results. Secondly, data was collected with the drones being flown approximately radially back and forth with respect to the radar to try to keep the target within the antenna beam. In some cases, the antenna pointing was adjusted live during the flights. Deriving the RCS values from the hovering data is straightforward and the results are obtained from the single range bin corresponding to the target. For the flying data, the drone is first tracked by using a peak search to find the range

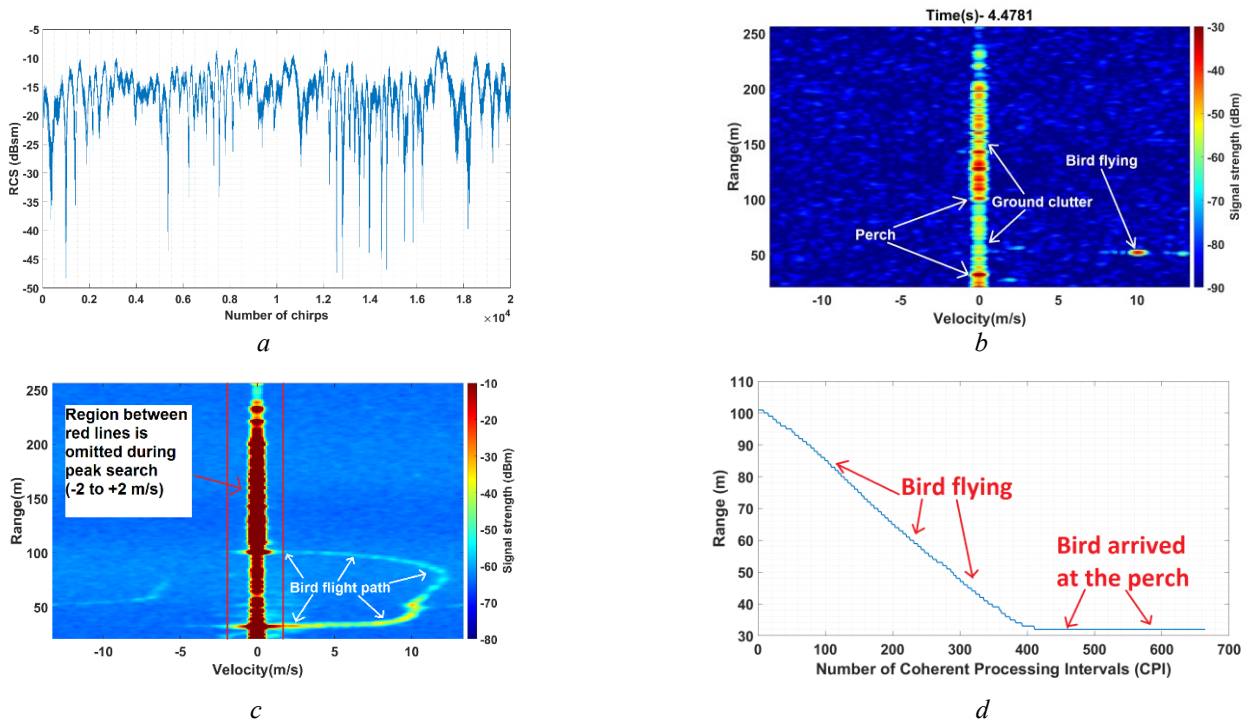


Figure 3: (a) Example K-band RCS plot of a DJI Inspire 1 as a function of chirp number, illustrating chirp-to chirp RCS fluctuation, (b) Example K-band range-Doppler profile showing the bird flying at 10 ms^{-1} , (c) Superposition of successive K-band range-Doppler profiles showing the flight trace, (d) Plot of the trace of the flying bird obtained from the range-Doppler profiles. RCS is then calculated for the corresponding range-Doppler bins

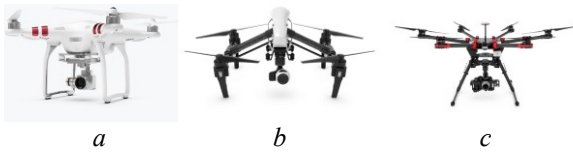


Figure 4: Drones used for data collection- (a) DJI Phantom 3 Standard, (b) DJI Inspire 1, (c) DJI S900

bin containing the maximum return power. The RCS is then derived from these bins. Fig. 3(a) shows an example RCS plot calculated for consecutive chirps. The plot shown here is obtained for a DJI Inspire 1 at K-band. It can be seen that the RCS fluctuations occur on a chirp-to-chirp basis. This characteristic has been consistent throughout the measurements of all the targets (drones and birds). As these targets are combinations of various independent scatterers, this suggests that the targets are of Swerling II type [19]. It should be noted that the drones were flown at a sufficient altitude to ensure that the multipath (along with clutter) is absent or negligible.

For the bird data collection it was not possible to make the birds hover in the air so measurements were made as they flew from perch to perch, in response to calls and bait from their handlers. The bird RCS is expected to vary more strongly with azimuthal angle as the geometrical shape will be very different. The quantitative variation has not been measured as falconry birds are only partially compliant targets in terms of their flight path. To maximise the duration of data collection runs it was only practical to have them fly approximately up and down the radar beam. If they had flown across the radar beam we would have not collected sufficient data, plus the existing radars are not capable of tracking a target moving rapidly in azimuth. Typically the birds flew quite close to the ground to minimise their energy expenditure by gliding, except during take-off and landing. Due to their proximity to the ground, ground clutter returns and multipath effect were quite strong so the peak search method described above could not be used for tracking. Instead, range-Doppler processing of the radar data has been used to find the appropriate range bins during the flight path. Accurate range-Doppler profiles were available as all the radars are coherent. In a range-Doppler profile, the clutter is present in different velocity bins whereas the multipath will be present in different range bins. So, by carefully tracking the bird flight path and taking the absolute power values of the corresponding range/velocity bin from the range-Doppler profile, the effect of multipath is mitigated significantly. Fig. 3(b) shows an example of such a range-profile. The ground clutter and the perches (at 30 m and 100 m) are in the zero-Doppler region. Due to its bulk velocity, the bird is now easily separated from the clutter. Fig. 3(c) shows the trace of the bird's flight by adding all the consecutive range-Doppler plots. Due to the addition, the ground clutter signal strength appears stronger here than the true value. Fig. 3(d) is the track plot showing the range bins occupied by the bird at any given range-Doppler profile. This plot is obtained by using the peak search method at the non-zero Doppler region along the range-Doppler profiles. To avoid getting inaccurate range values, near-zero velocities about both sidebands of the zero-Doppler ($\pm 2 \text{ ms}^{-1}$) are omitted during the maximum signal search, as seen in Fig. 3(b). Also, only the values when the

bird was flying are used. As seen in Fig. 3(c), the flat line is when the bird is sitting on the perch and the bird is in the zero-Doppler region. These values are not used for the RCS measurement process.

The chirp period was set to $144 \mu\text{s}$ for NIRAD, $80.5 \mu\text{s}$ for T-220 and $234.8 \mu\text{s}$ for the 24 GHz system. These values correspond to chirp repetition frequencies (CRF) of 6.94 kHz, 12.4 kHz and 4.25 kHz, respectively. At 94 GHz, only the T-220 system was used for flying data collection due to its slightly relaxed beamwidth. The maximum unambiguous velocity range is then $\pm 9.93 \text{ ms}^{-1}$ at 94 GHz and $\pm 13.3 \text{ ms}^{-1}$ at 24 GHz. In both the T-220 and the 24 GHz radar, a single range-Doppler profile is obtained by processing 128 consecutive chirps, which is the coherent processing interval (CPI). For every CPI, the RCS of the flying bird is then calculated by taking the signal strength of the corresponding range. This way, the RCS is measured at every range-Doppler frame, instead of every chirp. It should be noted that appropriate corrections are used to obtain the absolute received power. FFT gain and window gain corrections have been imposed in both fast and slow time. For amplitude accuracy, a Flattop window has been used to obtain the range profiles. The values in dBm are finally converted to dBsm by using the calibration curves.

3. Drone RCS

This work has been concerned with consumer drones which fall under the category of "small unmanned aerial vehicles" which in the UK, according to CAA guidance document CAP 722, are for drones weighing less than 20 kg. Two quadcopters and a hexacopter were used for the RCS measurements. All the drones are made by DJI, the most popular commercial drone manufacturer. The model and size of the drones are as follows-

- *DJI Phantom 3 Standard* (weight 1.216 kg, width 35 cm, blade length 13 cm)
- *DJI Inspire 1* (weight 2.845 kg, width 58 cm, blade length 34.5 cm)
- *DJI S900* (weight 3.3 kg, width 90 cm, blade length 38.1 cm)

The physical structures of the drones can be seen in Fig. 4. It can be seen that the main body (excluding the gimbal) of the Inspire is not symmetrical, unlike the other two. The drones were always flown at least 7 m above the ground and no further than 150 m range to minimise clutter returns from the ground and distant trees. Care has been taken to ensure that only those data were considered where the targets were well within the radar beam. On average, a typical measurement run was about 5-7 s long, accumulating more than 20,000 chirps in a single dataset for any given radar.

Fig. 5 shows the RCS values of the DJI Phantom 3 Standard at 94 GHz. For all the RCS histogram plots, the corresponding cumulative distribution function (CDF) curves are overlaid. In Fig. 5 (a,b), the drone was hovering 102.5 m away from the radar and 12 m above the ground. The data was obtained with NIRAD. The RCS modal value is -17 dBsm in one case and -23 dBsm in the other. In both cases, a secondary peak in the histogram is observed at around 6-8 dB higher than the modal value. This phenomenon is often observed in the case of the Phantom but not all the time. We suggest this is because the propeller blades of the Phantom, which are quite close to each other and to the fuselage,

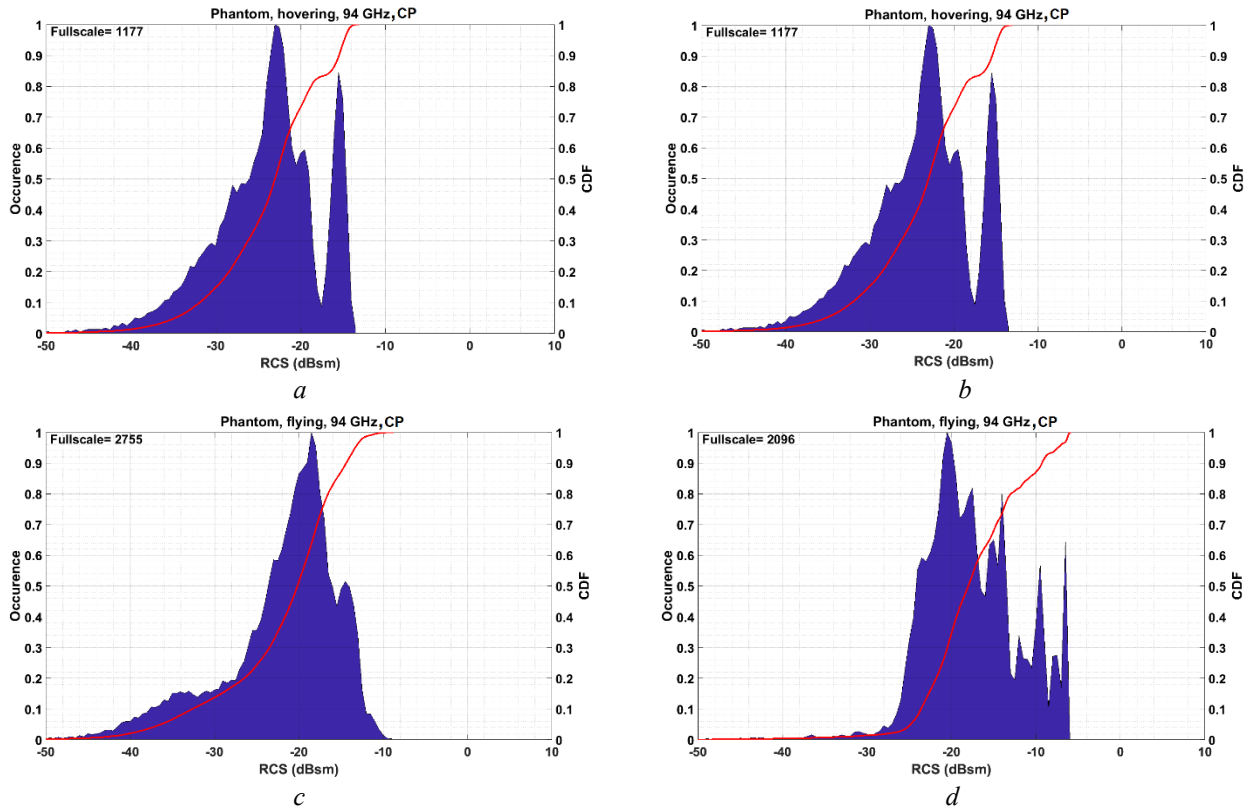
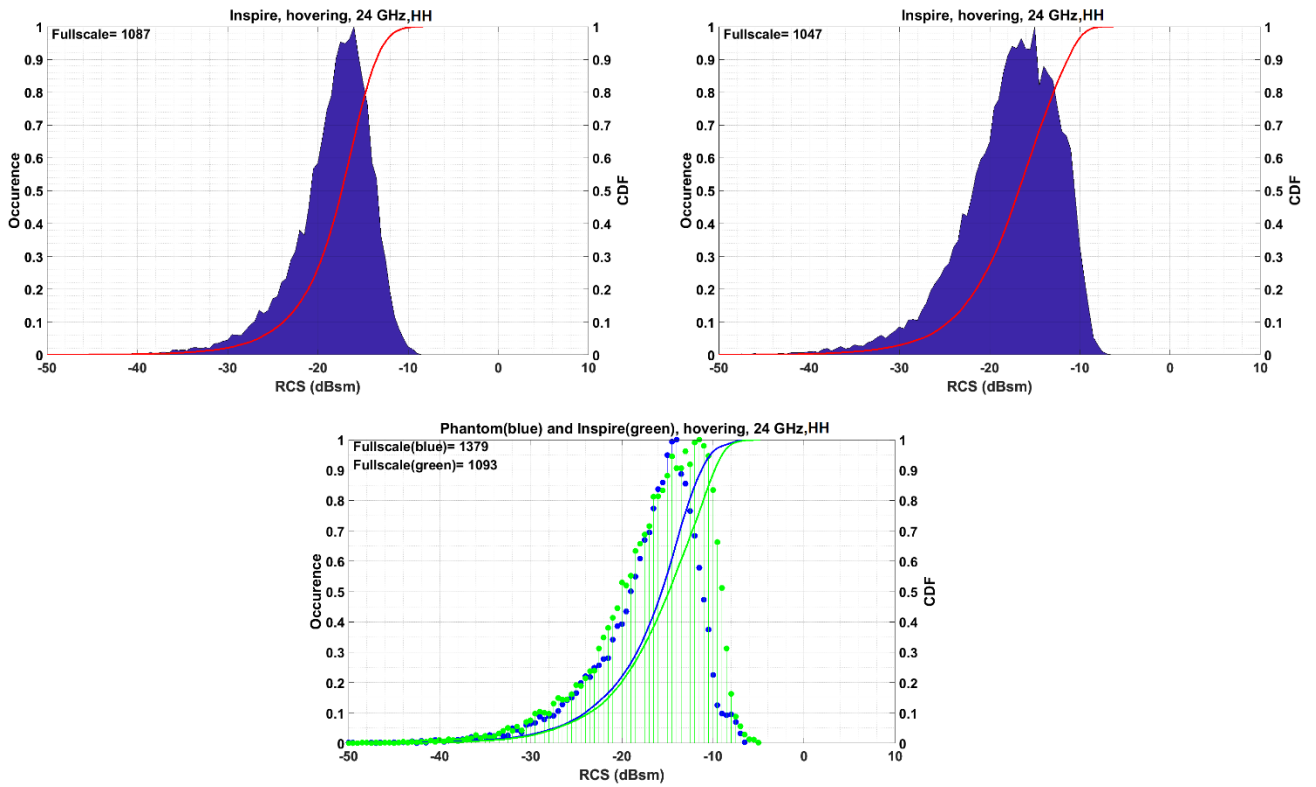


Figure 5: (a)-(b) RCS histograms and the corresponding CDF plots of DJI Phantom 3 Standard hovering at 94 GHz showing distinct secondary peaks, (c)-(d) RCS histograms and the corresponding CDF plots of DJI Phantom Standard 3 flying at 94 GHz

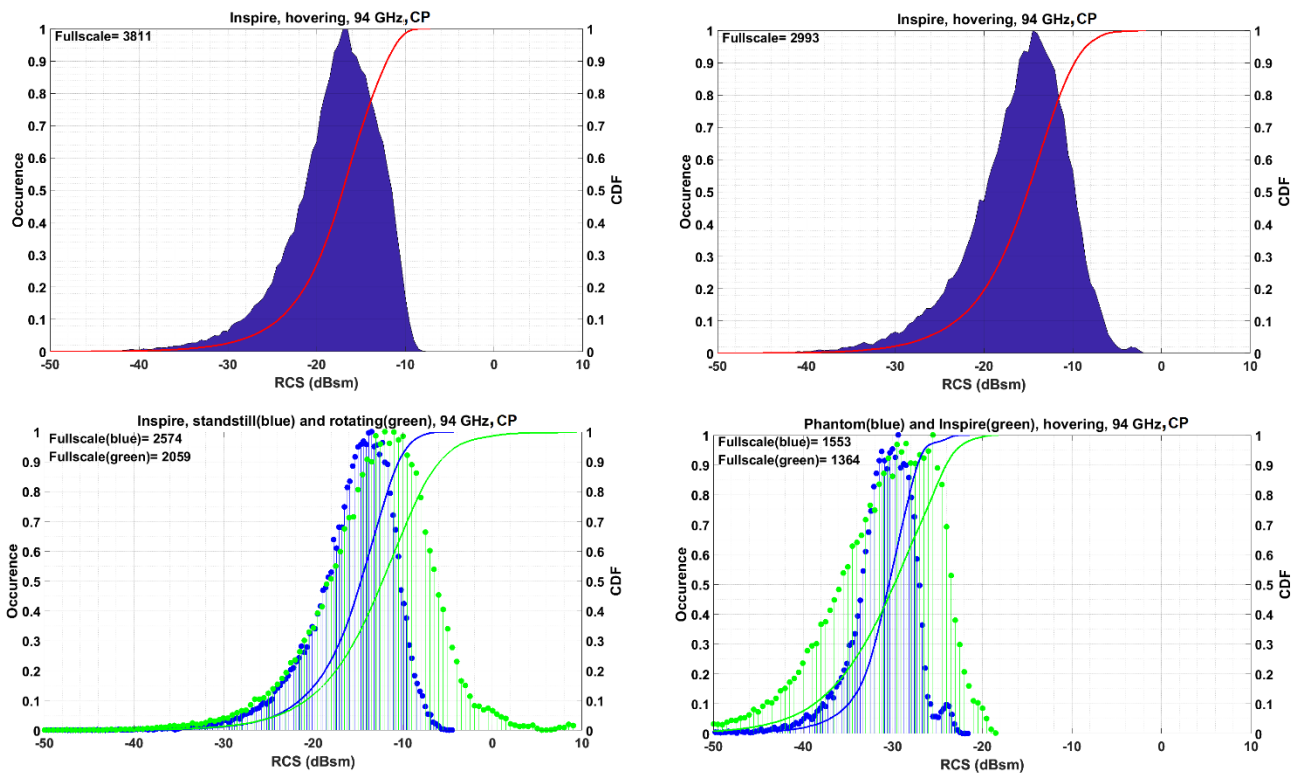
sometimes line up and increase the overall return signal. Separate measurements of this drone, when suspended on nylon monofilament, with propellers stationary and spinning, also showed that the secondary peak is only evident when the propellers are spinning, confirming this hypothesis. Similar observation and postulation regarding the RCS increase due to propeller motion has been made in [20], [21]. Fig. 5 (c,d) show RCS values when the Phantom was flying back and forth between approximately 60 and 80 m. Here, the data was obtained with T-220. The RCS modal values are -18 dBsm and -20 dBsm. Note that the distribution becomes slightly wider when the drone is flying (as seen in Fig. 5(d)). From these four examples, it can be seen that the RCS modal value for the DJI Phantom 3 Standard is around -20 ± 3 dBsm and the maximum RCS value is around -11 ± 3 dBsm at 94 GHz. The variations in these data sets are principally attributed to differences in aspect angle. The range of in-flight RCS values for this drone at 94 GHz, accounting for variations in aspect angle, typically falls between -30 and -10 dBsm using the 10 % and 90% points of the CDF. Further quantitative analysis of the RCS distribution is done in section 5.

Fig. 6(a) shows the RCS distribution of the hovering DJI Inspire 1 and DJI Phantom 3 Standard at 24 GHz. The top two histograms show that the modal RCS of the Inspire is around -15 to -16 dBsm for two measurement runs. The drone was hovering 89 m away from the radar at 22.2 m altitude. The bottom histogram was obtained by having both the Inspire and the Phantom hovering simultaneously. The Inspire was 86 m away from the radar at 13 m altitude whilst the Phantom was at 71 m range and at 10 m altitude. The modal RCS of the Phantom and Inspire are -14 dBsm and -11 dBsm respectively. In both cases the values are higher than in

the preceding histograms. This may be due to ground clutter as the 24 GHz radar elevation beamwidth is quite large and the altitude of the drones had to be reduced to keep both of them properly within the beam. In Fig. 6(b), two example RCS distribution plots of the DJI Inspire 1 at 94 GHz (T-220) are shown. The modal RCS is -16 dBsm in the first one and -14 dBsm in the other. The drone was hovering at 85 m range and at 8 m altitude. The bottom left histogram plot compares the Inspire hovering with the body stationary and then rotating through 360° in azimuth whilst hovering. The RCS peak increases by about 2 dB along with 5 dB increase in histogram width, when the whole fuselage is rotating (slowly) whilst the drone is hovering in one spot. We believe this reflects the variation in RCS with azimuth angle as would be expected given its body geometry. In Fig. 4, it can be seen that the Inspire has relatively asymmetrical geometrical shape compared with the other two drones (it has a long, thin fuselage). The bottom right histogram is for the Phantom and Inspire measured at 94 GHz (T-220). As the beam is very narrow in azimuth for that radar, neither of the drones were properly within the beam hence the very low RCS values. Nonetheless, a relative comparison can be made and the modal RCS of the Inspire is 6 dB higher than the Phantom. This illustrates the fact that in real scenarios the RCS values will fluctuate quite a lot due to the dynamic environment. Histogram plots in Fig. 7 compare flying data of the Inspire at 24 and 94 GHz. The flying range was about 70-100 m. At 24 GHz, the modal RCS is -12 dBsm whereas at 94 GHz (T-220), it is -17 dBsm. The 5 dB lower value at 94 GHz is because data were taken simultaneously with both radars and T-220 has a sufficiently narrow azimuth beamwidth that the drone was not always entirely within the beam.



a



b

Figure 6: (a) RCS Histograms and the corresponding CDF plots of DJI Inspire 1 and DJI Phantom 3 Standard hovering at 24 GHz, (b) RCS Histograms and the corresponding CDF plots of DJI Inspire 1 and DJI Phantom 3 Standard hovering at 94 GHz. RCS is measured for different scenarios (hovering individually, hovering simultaneously, hovering while rotating on its axis) to illustrate the variations in dynamic scenarios

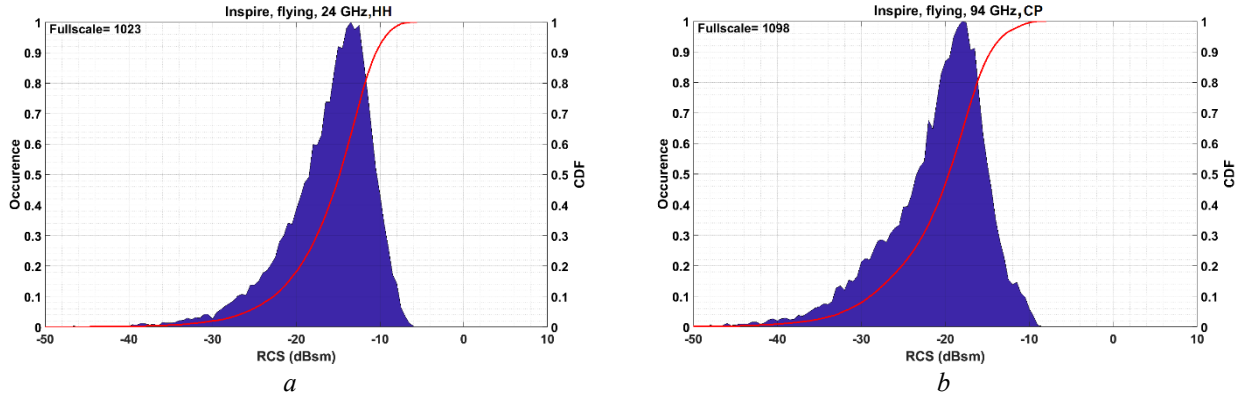


Figure 7: (a) RCS Histogram and the corresponding CDF plot of DJI Inspire 1 flying at 24 GHz, **(b)** RCS Histogram and the corresponding CDF plot of DJI Inspire flying at 94 GHz

Fig. 8 shows that the RCS of the hexacopter (DJI S900) is highest of the three, as expected due to its size. In Fig. 8(a) for 24 GHz, the drone was hovering at 60 m range and at 12 m altitude. The modal RCS at 24 GHz is -8 dBsm. In Fig. 8(b), the modal RCS is -8 to -10 dBsm at 94 GHz (T-220). The hexacopter was hovering here as well. Slight sideways motion of the drone was present as it is manually controlled, unlike the other two which hover automatically. This accounts for the slightly wider peak at 94 GHz.

Fig. 8(c,d) show the RCS distribution when the hexacopter is flying. The flying range was about 50-60 m from the radar. At 24 GHz, the peak RCS is -8 dBsm (seen in Fig. 8(c)) and -9 dBsm at 94 GHz (seen in Fig. 8(d)).

4. Bird RCS

The details of the birds used for the data collection are as follows-

- *Northern Hawk Owl* (weight 0.26 kg, length 40 cm, wingspan 45 cm)
- *Harris Hawk* (weight 0.71 kg, length 55 cm, wingspan 115 cm)
- *Indian Eagle Owl* (weight 0.97 kg, length 52 cm, wingspan 135 cm)
- *Tawny Eagle* (weight 1.84 kg, length 65 cm, wingspan 175 cm)

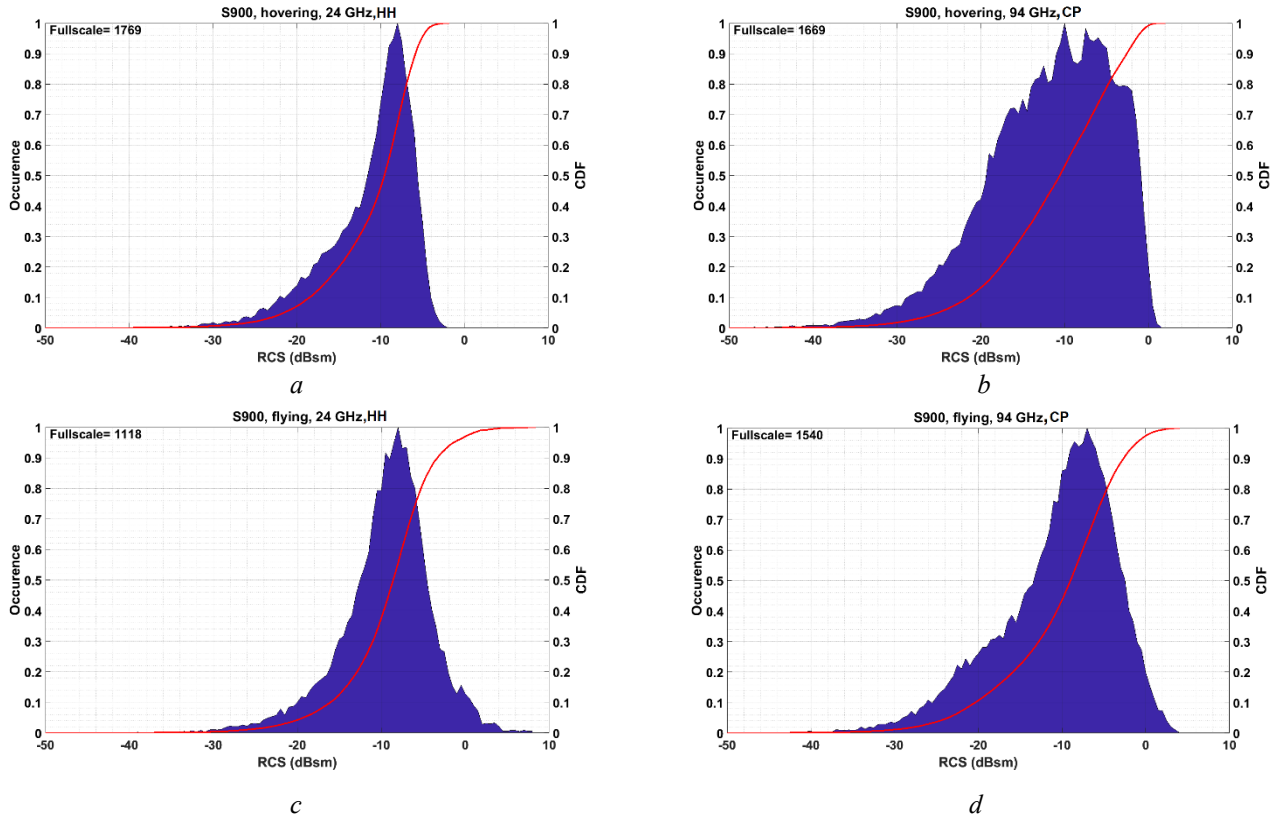


Figure 8: (a) RCS Histogram and the corresponding CDF plot of DJI S900 hovering at 24 GHz, **(b)** RCS Histogram and the corresponding CDF plot of DJI S900 hovering at 94 GHz, **(c)** RCS Histogram and the corresponding CDF plot of DJI S900 flying at 24 GHz, **(d)** RCS Histogram and the corresponding CDF plot of DJI S900 flying at 94 GHz

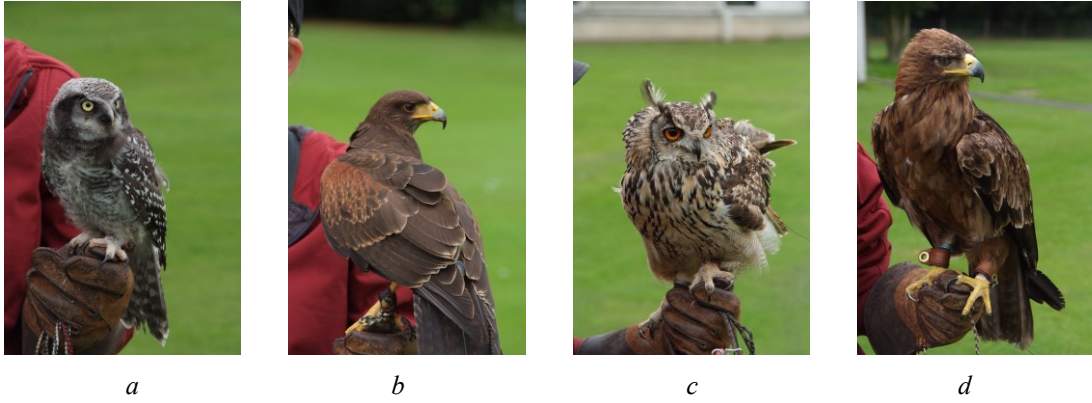


Figure 9: Birds used for data collection- (a) Northern Hawk Owl, (b) Harris Hawk, (c) Indian Eagle Owl, (d) Tawny Eagle

Fig. 9 shows the images of these birds. Different sizes of birds were chosen intentionally to investigate a range of RCS values. For the bird data analysis Doppler processing is done to evaluate the presence of the bird within the radar beam in each dataset. The birds were made to fly from one perch to the other, but the flight path in between could not be controlled which depended on the wind and the mood of the birds. Hence just having a straight line between the radar beam and the perches did not always guarantee decent data. Lots of trials were taken to ensure good data for all the birds. All the bird RCS measurements were taken with the birds facing along the line (both forward and backward) of the radar beam. During flight, the birds tend to glide to conserve energy. They flap wings mostly during take-off and landing. As can be seen from the Fig. 3(c), the return signal from the bird

increases slightly when it starts to flap wings (while approaching the perch) as the surface area for radar reflection increases.

Fig. 10 shows the RCS distribution of the Northern Hawk Owl flying, at both K-band and W-band. The bird flew between the high perch (30 m range) and the low perch (50 m range), in both directions. As the bird is quite small, the distance has been kept short. Fig. 10(a) shows that the RCS modal value is -30 dBsm at 24 GHz. Fig. 10(b) reveals the RCS at 94 GHz is about 2 dB lower. The width of the RCS distribution at 24 GHz appears wider than at 94 GHz but this is likely to be an experimental artefact. The Northern Hawk Owl flew a curved flight path which caused this variation in received power.

The Harris Hawk flight path was straighter which meant it remained within both radar beams all the time yielding more reliable data. Fig. 11 shows the RCS distribution of the Harris Hawk is about 10 dB higher than that of the Northern Hawk Owl. The modal RCS at 24 GHz is -22 dBsm, as seen in Fig. 11(a) whilst at 94 GHz, it is -20 dBsm, as shown in Fig. 11(b).

Fig. 12 shows the results for the Indian Eagle Owl. Fig. 12(a) shows that the modal RCS is -21 dBsm at 24 GHz whilst Fig. 12(b) shows it is -20 dBsm at 94 GHz.

Finally, the RCS distribution of the Tawny Eagle can be seen in Fig. 13(a) for 24 GHz and Fig. 13(b) for 94 GHz. In both frequency bands, the modal RCS is observed to be -18 dBsm.

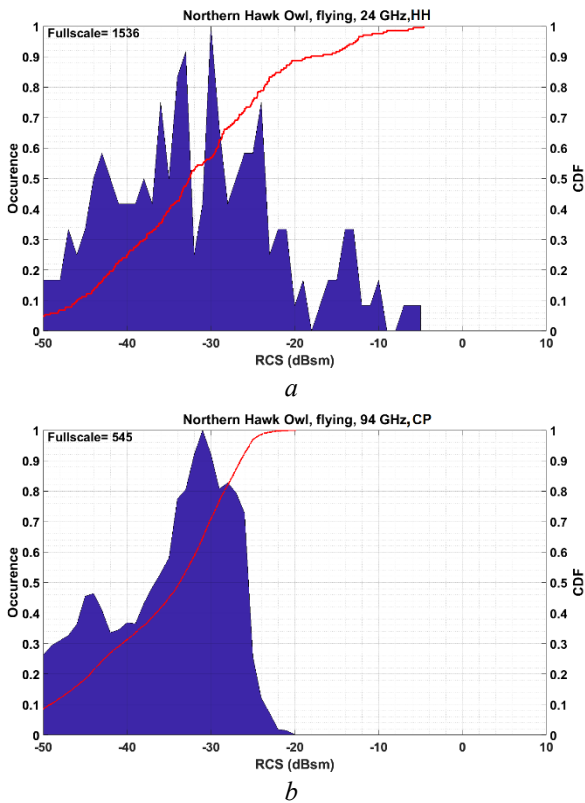


Figure 10: (a) RCS histogram and the corresponding CDF plot of Northern Hawk Owl flying at 24 GHz, (b) RCS histogram and the corresponding CDF plot of Northern Hawk Owl flying at 94 GHz

5. RCS data analysis

While analysing the histogram shapes of all the targets, bimodal distributions are often observed for the birds. From the drone data, the secondary peak is mainly observed for the Phantom but not for the other two. The conjecture is that the propeller blades are comparatively far away from each other and the body for both the Inspire and the S900 (as seen in Fig. 4) so the effect of propeller alignment in enhancing RCS is negligible. On the other hand, in Fig. 13, a notable secondary peak in the RCS distribution is observed for the Tawny Eagle in the region between -10 dBsm and +5 dBsm, which is higher than the modal RCS. A slight hint of a secondary peak is also observed in Fig.12 for the Indian Eagle Owl. In the case of the Harris Hawk and the Northern Hawk Owl, this secondary high RCS peak is not apparent at all. We conjecture that this

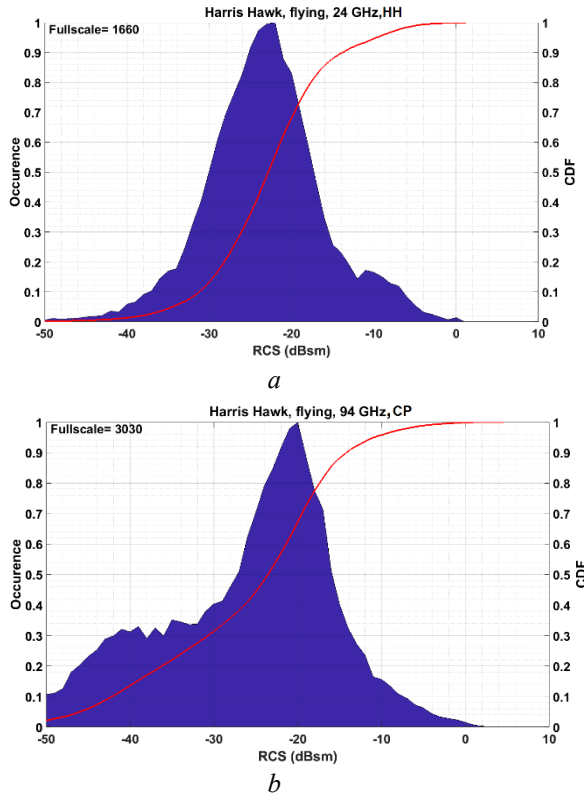


Figure 11: (a) RCS histogram and the corresponding CDF plot of Harris Hawk flying at 24 GHz, (b) RCS histogram and the corresponding CDF plot of Harris Hawk flying at 94 GHz

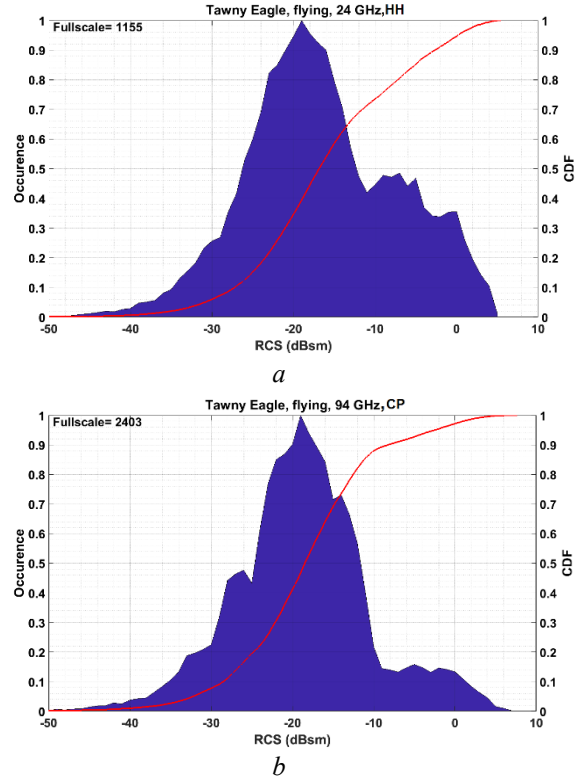


Figure 13: (a) RCS histogram and the corresponding CDF plot of Tawny Eagle flying at 24 GHz, (b) RCS histogram and the corresponding CDF plot of Tawny Eagle flying at 94 GHz

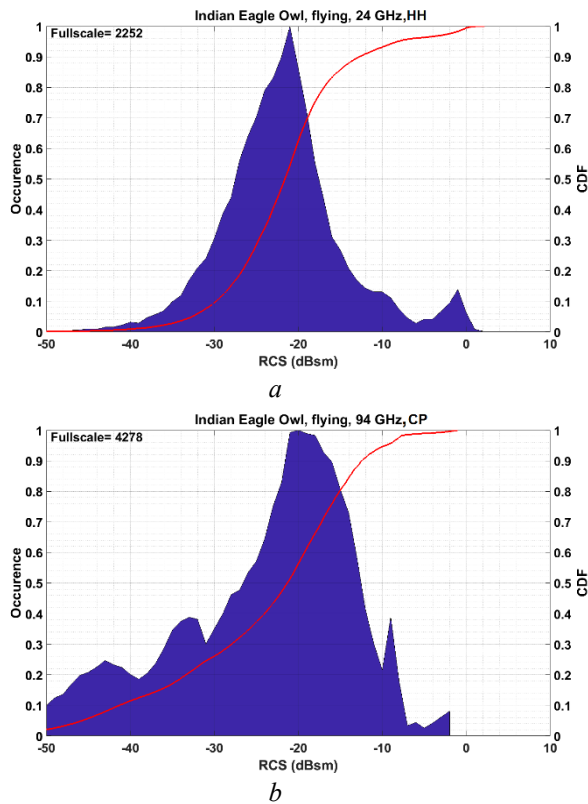


Figure 12: (a) RCS histogram and the corresponding CDF plot of Indian Eagle Owl flying at 24 GHz, (b) RCS histogram and the corresponding CDF plot of Indian Eagle Owl flying at 94 GHz

phenomenon can be attributed to the wing flapping of the birds, particularly the larger species. When the large birds are flapping wings, especially when decelerating before landing, the wing faces are often orthogonal to the ground and facing the radar due to the radial flight paths, hence increasing the overall presented surface area. This effect is particularly obvious in the Tawny Eagle histogram plots. In contrast, the wing flapping pattern of small birds (i.e. Northern Hawk Owl) is different and their wing faces stay more parallel to the ground when flapping, with less variation in projected area and hence RCS.

Table 1 provides a quantitative summary of the RCS values. The table amalgamates data from both hovering and flying drones to demonstrate the dynamic RCS variation. It is seen that for all targets, the modal RCS, maximum RCS and the CDF range are quite similar at 24 and 94 GHz. This is because all the targets are in the optical region of electromagnetic scattering. Just by considering the length of the main body of the targets, which accounts for most of the RCS, a simplistic calculation can be made to predict the scattering region. To be within the optical region, the condition $2\pi L/\lambda \gg 10$ has to be fulfilled, where L is the size or significant dimension of the target and λ is the radar wavelength [22]. If we consider the Northern Hawk Owl, which is the smallest target of all, for which L is 40 cm, $2\pi L/\lambda$ is 201 at 24 GHz and 787.5 at 94 GHz. In both cases, the criterion for scattering in the optical region is easily satisfied. Our results for the Phantom are consistent with those of [6] at X-band, for which the optical region is also valid.

As the polarisation of the radar systems used for the data collection are different, direct RCS comparison between the frequency bands is not straightforward. At both K- and

Table 1 RCS distribution summary (24 GHz- HH, 94 GHz- CP)

Target	Average modal RCS (dBsm)		Maximum RCS (dBsm)		Average CDF 10% and 90% points (dBsm)	
	24 GHz	94 GHz	24 GHz	94 GHz	24 GHz	94 GHz
Drones						
DJI Phantom 3 Standard	-20	-20	-6.2	-6	-29.5,-12	-27.5,-12
DJI Inspire 1	-15	-15	-5	-2	-24.5,-11.5	-23,-11
DJI S900	-8	-8	8	2	-17,-4.75	-21,-2.5
Birds						
Northern Hawk Owl	-30	-31	-5	-20	-45.5,-18	-49,-27.5
Harris Hawk	-22	-20	1	2.8	-32,-14	-42,-14
Indian Eagle Owl	-21	-20.5	2	-2	-30,-12.5	-41.5,-12.4
Tawny Eagle	-19	-19	5	7	-26,-2.5	-28,-8

W-bands, the polarisation dependence of the bulk RCS is likely to be a function of the projected frontal area of the target as seen by the radar, and probably dominated by the fuselage. In all these cases (drones and birds) we suggest that the aspect ratio of the target in flight may be slightly wider in azimuth than in elevation (as seen in Fig. 4), so this could cause the HH RCS to be slightly larger than the VV RCS. The CP RCS will therefore be intermediate between the two linear cases. However, none of the targets can be considered ‘long and thin’, so a strong polarisation dependence is not expected and there might be only a few dB difference at most between HH, CP and VV at any frequency. The values in Table 1 shows that 24 GHz HH and 94 GHz CP values are mainly within a few dB for each target.

Table 1 also shows that there is a clear trend in the RCS with increasing target size. The modal RCS increases from -20 dBsm (Phantom) to -15 dBsm (Inspire) and then to -8 dBsm (S900). In case of the birds, the modal RCS of the Northern Hawk Owl is the lowest (-30 dBsm) and the Tawny Eagle is the highest (-19 dBsm).

The maximum RCS values can be used to predict upper bounds for target detection. In general the maximum RCS is within a few dB between 24 and 94 GHz. However, an obvious discrepancy exists for the Northern Hawk Owl with values of -5 dBsm at 24 GHz versus -20 dBsm at 94 GHz. This is likely to be due to ground clutter affecting the measured RCS at 24 GHz whilst the 94 GHz values may have been suppressed due to the target falling out of the narrow beam.

The CDF 10% and 90% value ranges broadly reflect the trend seen in the modal RCS values, with an increase in overall RCS corresponding to an increase in the target size. These values represent the most commonly occurring range of RCS values which will be useful for predicting the likely range of expected values encountered when using radars at 24 and 94 GHz to detect drones and birds of the sizes measured.

Supplementary data has been provided in the appendix consisting of some more RCS histogram plots of the drones in different settings.

6. Conclusion

RCS values are of great importance in terms of target detection and classification, especially in security applications. More so, it is necessary to characterize the RCS values of these target of interests in a dynamic environment, as those values will be used most of the time during real time processing. The goal of this paper was to collect and process RCS data of drones and birds at high frequencies (K-band and

W-band). The experimental setup has been intentionally chosen such that it corresponds to a realistic scenario for a drone/bird detection radar system. The practical factors such as the target movement and clutter have been considered during this study. The aim was to analyze the RCS distribution of the targets in such cases. This was done to determine whether the RCS values can be used reliably to identify or discriminate a target in a real life, fast changing situation (i.e. urban environment).

There is a potential to design and build low-cost compact drone detection radar systems at K-band and W-band because of the commercial availability of chips at these frequencies. Knowledge of RCS properties of these targets at these frequencies will be very useful for system design.

The experimental data analysis reveals that drones and birds have RCS values which scale broadly with size, but in all cases are large enough to be detected by suitably sensitive radars. The experimental results in this paper also show that at K-band and W-band, drones and birds fall in the optical scattering region and the RCS values are similar at both frequencies. An overlap in RCS values of the drones and birds is observed, due to the fact that they are quite similar in terms of physical size. The CDF 10% to 90% values can be used as bounding values for radar system design predictions. However, due to the similarity in RCS values of drones and birds, RCS values on their own cannot be reliably used for discriminating a drone from a bird. Other features of the targets (i.e. micro-Doppler) must be used along with the RCS information to achieve robust classification.

The RCS data presented in this paper can be used as a useful reference for predicting the performance of K-band and W-band drone detection radars and classification algorithms. Additionally, the bird RCS values at these frequencies could be used for applications other than drone detection such as a bird detecting radar for airspace surveillance or for the ecological monitoring of birds.

7. Acknowledgments

The authors acknowledge the funding received from the Science and Technology Facilities Council which has supported this work under grant ST/N006569/1. The authors thank their colleagues from the University, Dr Robert I. Hunter, Adeola Fabola and Dr Patrick Pomeroy for operating the drones. Also, the authors thank Elite Falconry, Kirkcaldy, for flying the birds.

8. References

- [1] “FAA Says Drone Usage Will Triple by 2020 - Business Insider.” [Online]. Available: <http://www.businessinsider.com/faa-says-drone-usage-will-triple-by-2020-2016-3?IR=T>. [Accessed: 20-Dec-2017].
- [2] S. Rahman and D. A. Robertson, “Millimeter-wave micro-Doppler measurements of small UAVs,” in *Proc. SPIE 10188, Radar Sensor Technology XXI*, 2017, vol. 10188, p. 101880T.
- [3] P. Molchanov, R. I. A. Harmanny, J. J. M. de Wit, K. Egiazarian, and J. Astola, “Classification of small UAVs and birds by micro-Doppler signatures,” *Int. J. Microw. Wirel. Technol.*, vol. 6, no. 3–4, pp. 435–444, 2014.
- [4] D. Tahmouh, “Detection of small UAV helicopters using micro-Doppler,” in *Proc. SPIE 9077, Radar Sensor Technology XVIII*, 2014, vol. 9077, p. 907717.
- [5] M. Ritchie, F. Fioranelli, H. Griffiths, and B. Torvik, “Monostatic and bistatic radar measurements of birds and micro-drone,” in *2016 IEEE Radar Conference (RadarConf)*, 2016, pp. 1–5.
- [6] A. Schroder *et al.*, “Numerical and experimental radar cross section analysis of the quadcopter DJI Phantom 2,” in *2015 IEEE Radar Conference*, 2015, pp. 463–468.
- [7] M. Ritchie, F. Fioranelli, H. Griffiths, and B. Torvik, “Micro-drone RCS analysis,” in *2015 IEEE Radar Conference*, 2015, pp. 452–456.
- [8] J. L. Volakis, A. (Arindam) Chatterjee, and L. C. Kempel, *Finite element method for electromagnetics: antennas, microwave circuits, and scattering applications*. IEEE Press, 1998.
- [9] R. F. Harrington, “Matrix methods for field problems,” *Proc. IEEE*, vol. 55, no. 2, pp. 136–149, 1967.
- [10] A. Taflove and S. C. Hagness, *Computational electrodynamics: the finite-difference time-domain method*. Artech House, 2005.
- [11] E. F. Shaeffer, J. F. Tuley, and M. T. Knott, *Radar Cross Section*. Institution of Engineering and Technology, 2004.
- [12] P. Blacksmith and R. B. Mack, “On measuring the radar cross sections of ducks and chickens,” *Proc. IEEE*, vol. 53, no. 8, pp. 1125–1125, 1965.
- [13] D. Mirkovic, P. M. Stepanian, J. F. Kelly, and P. B. Chilson, “Electromagnetic Model Reliably Predicts Radar Scattering Characteristics of Airborne Organisms,” *Sci. Rep.*, vol. 6, no. 1, p. 35637, Dec. 2016.
- [14] B. Torvik, K. E. Olsen, and H. D. Griffiths, “X-band measurements of radar signatures of large sea birds,” in *2014 International Radar Conference*, 2014, pp. 1–6.
- [15] B. Torvik, K. E. Olsen, and H. D. Griffiths, “K-band radar signature analysis of a flying mallard duck,” in *International Radar Symposium, IRS 2013. Volume II: Dresden, Germany, June 19-21, 2013: proceedings*, 2013.
- [16] D. A. Robertson and S. L. Cassidy, “Micro-doppler and vibrometry at millimeter and sub-millimeter wavelengths,” in *Proc. SPIE 8714, Radar Sensor Technology XVII*, 2013, vol. 8714, p. 87141C.
- [17] D. A. Robertson, G. M. Brooker, and P. D. L. Beasley, “Very low-phase noise, coherent 94GHz radar for micro-Doppler and vibrometry studies,” in *Proc. SPIE 9077, Radar Sensor Technology XVIII*, 2014, vol. 9077, p. 907719.
- [18] S. Rahman and D. A. Robertson, “Coherent 24 GHz FMCW radar system for micro-Doppler studies,” in *Proc. SPIE 10633, Radar Sensor Technology XXII*, 2018, no. 10633.
- [19] M. I. (Merrill I. Skolnik, *Introduction to radar systems*. McGraw Hill, 2001.
- [20] M. A. Govoni, “Micro-Doppler signal decomposition of small commercial drones,” in *2017 IEEE Radar Conference (RadarConf)*, 2017, pp. 0425–0429.
- [21] R. Guay, G. Drolet, and J. R. Bray, “Measurement and modelling of the dynamic radar cross-section of an unmanned aerial vehicle,” *IET Radar, Sonar Navig.*, vol. 11, no. 7, pp. 1155–1160, Jul. 2017.
- [22] N. C. Currie, R. D. Hayes, and R. N. Trebits, *Millimeter-wave radar clutter*. Artech House, 1989.

9. Appendix

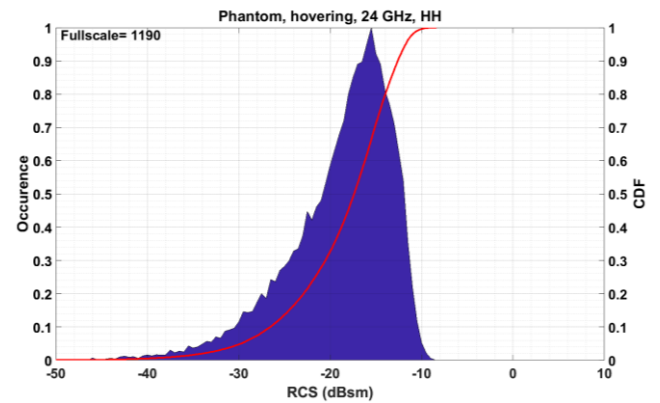


Figure A1: RCS histograms and the corresponding CDF plot of DJI Phantom 3 standard hovering at 24 GHz

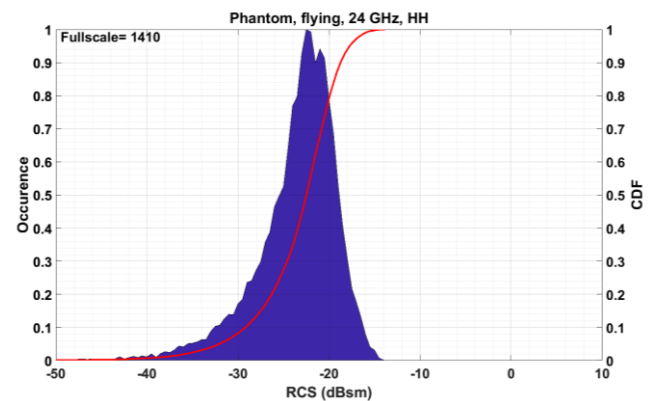


Figure A2: RCS histograms and the corresponding CDF plot of DJI Phantom 3 standard flying at 24 GHz

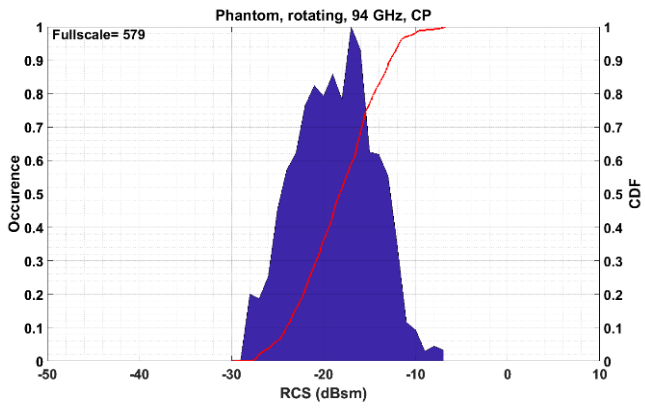


Figure A3: RCS histograms and the corresponding CDF plot of DJI Phantom 3 standard hovering while rotating on its axis at 24 GHz

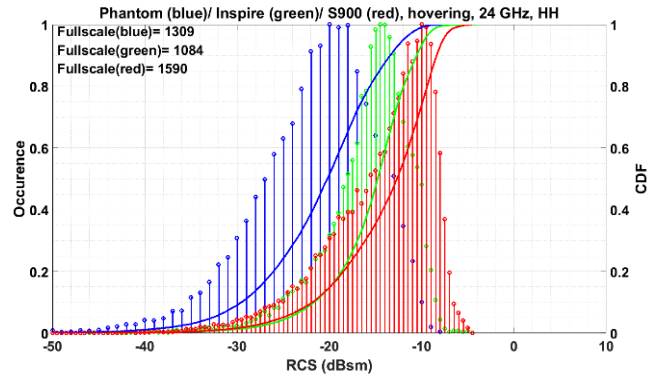


Figure A6: Overlaid RCS histograms and the corresponding CDF plots of DJI Inspire 1, DJI Phantom 3 Standard and DJI S900 hovering at 24 GHz

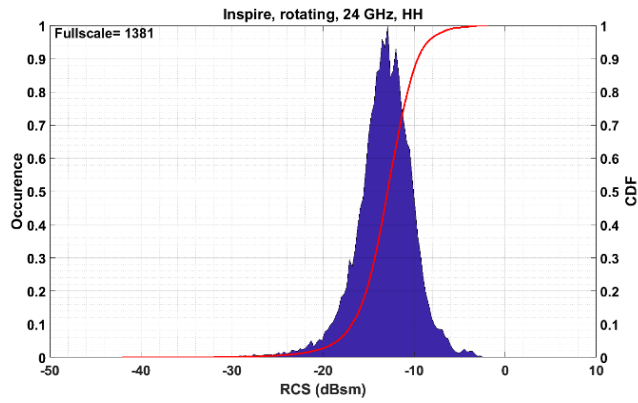


Figure A4: RCS histograms and the corresponding CDF plot of DJI Inspire 1 hovering while rotating on its axis at 24 GHz

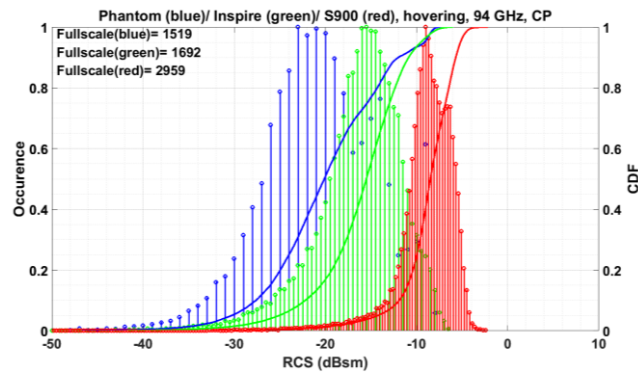


Figure A5: Overlaid RCS histograms and the corresponding CDF plots of DJI Inspire 1, DJI Phantom 3 Standard and DJI S900 hovering at 94 GHz